*AGU Advances*

Original Version of

# Very low frequency earthquakes in between the seismogenic and tremor zones in Cascadia?

Wenyuan Fan[1], Andrew J. Barbour[2], Jeffrey J. McGuire[2], Yihe Huang[3], Guoqing Lin[4], Elizabeth S. Cochran[5], & Ryo Okuwaki[6]

[1] Scripps Institution of Oceanography, UC San Diego, La Jolla, California, USA
[2] U.S. Geological Survey, Earthquake Science Center, Moffett Field, California, USA
[3] Department of Earth and Environmental Sciences, University of Michigan, Ann Arbor, Michigan, USA
[4] Rosenstiel School of Marine and Atmospheric Science, University of Miami, Miami, Florida, USA
[5] U.S. Geological Survey, Earthquake Science Center, Pasadena, California, USA
[6] Mountain Science Center, Faculty of Life and Environmental Sciences, University of Tsukuba, Tsukuba, Ibaraki, Japan

# Very low frequency earthquakes in between the seismogenic and tremor zones in Cascadia?

**Wenyuan Fan[1], Andrew J. Barbour[2], Jeffrey J. McGuire[2], Yihe Huang[3], Guoqing Lin[4], Elizabeth S. Cochran[5], & Ryo Okuwaki[6]**

[1]Scripps Institution of Oceanography, UC San Diego, La Jolla, California, USA
[2]U.S. Geological Survey, Earthquake Science Center, Moffett Field, California, USA
[3]Department of Earth and Environmental Sciences, University of Michigan, Ann Arbor, Michigan, United States
[4]Rosenstiel School of Marine and Atmospheric Science, University of Miami, Miami, Florida, USA
[5]U.S. Geological Survey, Earthquake Science Center, Pasadena, California, USA
[6]Mountain Science Center, Faculty of Life and Environmental Sciences, University of Tsukuba, Tsukuba, Ibaraki, Japan

**Peer-Review DISCLAIMER:**



**Key Points:**

- Three large VLFEs in Cascadia were dynamically triggered by teleseismic waves.
- These VLFEs occurred in between the seismogenic and tremor zones.
- The largest VLFE has a moment magnitude of 5.7.

Corresponding author: Wenyuan Fan, `wenyuanfan@ucsd.edu`

## Abstract

Megathrust earthquakes and their associated tsunamis cause some of the worst natural disasters. In addition to earthquakes, a wide range of slip behaviors are present at subduction zones, including slow earthquakes that span multiple orders of spatial and temporal scales. Out of all types of slow earthquakes, very low frequency earthquakes (VLFEs) are most similar to regular earthquakes, and understanding these events may shed light on the stress or strength conditions of the megathrust fault. However, the physical nature of VLFEs are poorly understood despite their frequent occurrence. Here we show three VLFEs in Cascadia that were dynamically triggered by a 2009 Mw 6.9 earthquake in the Gulf of California. The VLFEs likely locate in between the seismogenic zone and the Cascadia episodic tremor and slip (ETS) zone, including one event with a moment magnitude of 5.7. This is the largest VLFE reported to date, causing clear geodetic signals. Our results suggest that the Cascadia megathrust fault can slip rapidly in this gap zone, and such a permissible slip behavior would allow deeper penetrations of future great megathrust earthquakes in the region, indicating greater seismic hazards for the coastal communities. Further, the observed seismic sources may represent a new class of slip events, which characteristics do not fit current understandings of slow or regular earthquakes.



## Plain Language Summary

Megathrust earthquakes and their associated tsunamis pose significant hazards in Cascadia. In addition to earthquakes, episodic tremor and slip (ETS) events have been discovered in the region at depths of 30 to 50 km, 10–15 km below the seismogenic zone. The expected slip behavior between the seismogenic and ETS zones remains unknown, leaving the rupture extents of future megathrust earthquakes unclear. We detect and locate three very low frequency earthquakes (VLFEs) in this gap region, including one with a moment magnitude of 5.7. This is the largest VLFE reported to date, and its detection not only shows that the megathrust fault can slip rapidly in this gap zone but also challenges current understanding of slow earthquake physics.


## 1 Introduction

The Cascadia subduction zone poses serious earthquake and tsunami hazards to some of the most populous regions of the United States and Canada. Geological records reveal that at least 19 great megathrust earthquakes occurred in the region over the past ten thousand years [*Walton et al.*, 2021]. However, as an exceptionally seismically quiet subduction zone [*Wang and Tréhu*, 2016], large megathrust earthquakes in Cascadia have never been recorded by modern instrumentation. In contrast, slow earthquakes, which differ from regular earthquakes, occur frequently across the whole subduction zone [*Brudzinski and Allen*, 2007; *Gomberg et al.*, 2010]. These slow earthquakes encompass a wide spectrum of slip behaviors [*Peng and Gomberg*, 2010], including slow slip events (SSEs) [*Dragert et al.*, 2001], very low frequency earthquakes (VLFEs) [*Ghosh et al.*, 2015; *Hutchison and Ghosh*, 2016], low-frequency earthquakes (LFEs) [*Bostock et al.*, 2012; *Sweet et al.*, 2019], and non-volcanic seismic tremor [*Wech and Creager*, 2008; *Brown et al.*, 2009]. In Cascadia, slow slip events and seismic tremor often couple with each other as episodic tremor and slip (ETS) events [*Rogers and Dragert*, 2003; *Bartlow et al.*, 2011].

These ETS events recur semi-regularly and can propagate up to ~500 km from central Oregon, US, to Vancouver Island, Canada [*Wech and Bartlow*, 2014]. They can have moment magnitudes equivalent to Mw 6.7 earthquakes with the SSEs releasing most of their moments [*Dragert et al.*, 2001; *Kao et al.*, 2010]. Additionally, typical VLFEs in the region can have equivalent moment magnitudes ranging from 2.1 to 4.1 [*Ghosh et al.*, 2015; *Hutchison and Ghosh*, 2016; *Ide*, 2016]. These events accommodate a portion of the slip deficit at the subduction zone and concentrate along a band at depths of 30–50 km, about 10 to 15 km deeper than the downdip edge of the seismogenic zone [*Brudzinski and*

*Allen*, 2007; *Gomberg et al.*, 2010; *Wang and Tréhu*, 2016; *Walton et al.*, 2021]. In between the ETS zone and the seismogenic zone on the fault, there is a gap that is not fully locked, yet devoid of slow earthquakes [*Hyndman and Wang*, 1995; *Wang et al.*, 2003; *Brudzinski and Allen*, 2007; *Gomberg et al.*, 2010; *Priest et al.*, 2010; *Schmalzle et al.*, 2014]. Understanding the slip behaviors in this gap zone gives insight into the stress and strength conditions of the megathrust fault, and can lead to improved forecasting of future earthquake rupture scenarios [*Bruhat and Segall*, 2016; *Ramos and Huang*, 2019]. Studies of this gap zone are largely hindered by a lack of robust observations, or the loss of resolution of onshore instruments; hence, little is known about the nature of the gap zone or its relation to the locked zone and the ETS zone.

In a search of the USArray data from August to October 2009, we find that three VLFEs occurred over a 5-minute period. Two of the VLFEs likely occurred in the gap zone between the seismogenic locked zone and the ETS zone, and one is likely adjacent to the gap zone (Figure 1). Geodetic data confirm the best resolved event, with clear observations of static strains that are consistent with the seismically derived focal mechanism. The VLFEs coincide with surface wave arrivals of the August 2009 Mw 6.9 Canal de Ballenas earthquake, and we examine whether the VLFEs may have been triggered by the dynamic stresses from the passing waves. These events were also close to the onset area of the 2009 Cascadia ETS event and occur three days before its reported initiation [*Bartlow et al.*, 2011]. This spatiotemporal correlation between the VLFEs and ETS event suggests that these previously unknown VLFEs were either diagnostic of, or played a role in, the nucleation process of the 2009 Cascadia ETS event. Most importantly, identifying these VLFEs offers new insight into the physical nature of the gap zone.

## 2 Datasets and Methods

### 2.1 Detecting and Locating VLFEs in Cascadia

We use an array-based surface wave detector that is developed from the AELUMA (Automated Event Location Using a Mesh of Arrays) method [*de Groot-Hedlin and Hedlin*, 2015; *Fan et al.*, 2018]. Our approach is data-driven with few assumptions about the nature of the seismic sources. The AELUMA method can detect and locate seismic sources from intermediate-period Rayleigh waves, and it is particularly well-suited for detecting unconventional seismic sources that are commonly missed in standard catalogs [*Fan et al.*, 2019, 2020]. This is because the method applies to continuous waveforms and can detect and locate any source of seismic radiation without phase picks or knowing the source types [*Fan et al.*, 2018]. We follow the same data processing protocol outlined in *Fan et al.* [2018] and use the same empirical parameters that have been implemented to investigate stormquakes and submarine landslides in the Gulf of Mexico [*Fan et al.*, 2019, 2020]. The only difference is that we use 360 s time-window and 180 s time-step for the beamforming procedure instead of using the 600 s time-window and 300 s time-step as used in previous studies.

The method takes advantage of local coherence of the recorded signals, and then forms an inverse problem to locate the signal sources assuming the waves propagating along the great circle paths [*de Groot-Hedlin and Hedlin*, 2015; *Fan et al.*, 2018]. We first divide the large arrays into small subarrays, each comprising three stations. Second, tau-p beamforming analysis is applied to continuous data that are filtered in the 20 to 50 s period band to detect signals, and the detections are screened through a quality control procedure [see details in *Fan et al.*, 2018]. The records (LHZ component) are from available stations located in the contiguous US during the study period. Due to the signal to noise ratios and the quality control steps, not all records are used for the final location. Third, the remaining detections are grouped into non-overlapping clusters. Fourth, detections of each cluster are used to locate one seismic source and its location uncertainty is empirically estimated [*Fan et al.*, 2019, 2020]. During the location step, possible arrival angle anomalies are empirically corrected using earthquakes reported in the Global Centroid Moment Tensor Project [*Ekström et al.*, 2012]. Finally, the quality of each located seismic event is assessed to avoid duplicates and a catalog is populated with the located events.

We detected three seismic sources (E1, E2, and E3) in Cascadia soon after the 2009 Canal de Ballenas earthquake that are likely VLFEs (Figures 1,2). Due to the spatiotemporal correlation between the 2009 Canal de Ballenas earthquake and the detected sources, we hypothesize that the detected sources were triggered by the 2009 earthquake. We will discuss this hypothesis in later sections. These three VLFEs were detected by 84, 57, and 187 subarrays, respectively. In particular, E3 can be clearly seen in the record section when the traces are aligned with respect to its location (Figure 3). Their location uncertainties are shown as the dashed lines in Figure 2. The location uncertainty of the detected seismic sources are computed by examining the spatial structure of a suite of grids within a misfit threshold [*Fan et al.*, 2018]. Based on the optimal location, grids that can minimize the misfit values within 25% of the optimal value are taken as possible source locations [*Fan et al.*, 2018]. From the set of possible sources, we compute a distance covariance matrix and use its eigenvectors and eigenvalues to define a location uncertainty-ellipse with the optimal solution in the center [*Fan et al.*, 2018] (Figure 2). This approach can provide a formal way to address statistical location uncertainty due to data availability. However, the misfit threshold is chosen subjectively. In our case, the 25% of the optimal value is a conservative choice, and the results represent the lower-bound of the resolution. In later parts, we will evaluate the event locations with local strainmeter records, which provide independent constraints on the results.

### 2.2 Determining Focal-mechanism of the VLFEs

We use a cross-correlation method to estimate the focal-mechanism (Figure 4). The approach shares similarities with the grid-search centroid moment tensor inversion method, which has been applied to search VLFEs in Cascadia and offshore Japan [e.g., *Ito and Obara*, 2006; *Ghosh et al.*, 2015]. Our method resolves the event focal-mechanism, duration, and the event depth based on a VLFE catalog (Figure 4). Instead of searching the possible combinations of the fault geometry (strike, rake, dip) and event depth, we fix the E3 epicenter as the resolved location from our surface wave detector and use a VLFE catalog of events beneath southern Vancouver Island and northern Washington State [*Ide*, 2016] to forward calculate synthetic seismograms. Based on the amplitudes of the VLFE-related waves, we initially assume the event has a seismic moment of $2 \times 10^{18}\,\mathrm{N} \cdot \mathrm{M}$. The catalog has 112 events, and for each focal-mechanism (Figure 4), we compute three-component synthetic waveforms for sources at depth from 5 km to 50 km with a 5 km increment. We also investigate a set of source durations assuming a Gaussian function shape with the duration as 6 times the standard deviation; we test durations from 0.9 s to 257.1 s.

The synthetic waveforms are computed for each station at vertical, north-south, and east-west directions with the Instaseis method [*Driel et al.*, 2015]. The Instaseis method pre-computes a Green's function database with the axisymmetric spectral-element method AxiSEM [*Nissen-Meyer et al.*, 2014]. Here, we use the Green's functions calculated with the anisotropic version of the PREM model up to 5 s [*Dziewonski and Anderson*, 1981]. These synthetic seismograms are then filtered at 25 to 50 s period band and are cross-correlated with the observed three-component waveforms of the best-resolved event, E3, in the same frequency band. We use all available stations in the continental US with epicentral distances from 500 km to 3300 km (up to 30° epicentral distance, Figure 5). For each station, a representative cross-correlation coefficient is taken as the geometric mean of the cross-correlation coefficients of the three components (e.g., Figure 5), the preferred depth for the focal-mechanism maximizes the total summation of the representative cross-correlation coefficients from all stations. The optimal solution, including both the focal-mechanism and the event depth, has the maximum total summation of cross-correlation coefficients. After obtaining an optimal solution, we calculate the amplitude ratios between the synthetic waveforms and the observations for all the stations and component (Figure 4d), and the median value of the ratio distribution (0.25 for E3) is used to scale the initial seismic moment to compute for the VLFE moment.

Given the noise level of the records, we can only estimate the focal-mechanism for one of the detected seismic sources in Cascadia (E3), which has waveforms that are separated from the surface waves of the Canal de Ballenas earthquake (Figure 3). It is challenging to analyze events E1 and E2 in more detail because the high amplitude coda waves from the Canal de Ballenas earthquake construe the VLFE signal (Figure 3). The near-field stations in the Pacific Northwest (inset, Figure 1) are not used to analyze E3 due to the interference between its surface waves and those of the Canal de Ballenas earthquake (Figure S1).

### 2.3 Dynamic and Static Deformation

With our starting estimates that seismic moments of the VLFEs are on the order of $10^{18}$ N · M, geodetic methods may detect the associated static deformation and verify our results. We use strainmeters because they are generally sensitive to static strains from small-to-moderate crustal earthquakes, and can give precise onset timing of the static deformation, unlike with more commonly used space geodetic techniques (i.e., GNSS, InSAR). They can also measure broadband dynamic strains from the Canal de Ballenas event, which allows us to robustly estimate dynamic stresses at the times of the detected seismic sources. We will later examine the relations between the dynamic stress and the observed VLFEs.

In particular, we use strain data from borehole strainmeters (BSMs) in the Network of the Americas (NOTA) (Figure 6a) These BSMs are four-component Gladwin-type differential capacitance strainmeters [*Gladwin*, 1984]. Unprocessed data given in capacitance bridge counts are converted to linear strains using standard linearization procedure [*Barbour and Crowell*, 2017]. We outline the steps taken to analyze both dynamic strains from the source, and static strains from the VLFEs.

#### *2.3.1 Dynamic Strains from the Canal de Ballenas Source*

For analyses of the teleseismic waves, we analyze the root-mean-square strain timeseries $\epsilon$ for the given time window, given by $\epsilon = \sqrt{\left[g_1^2 + g_2^2 + g_3^2 + g_4^2\right]/4}$, where $g_1$ is the linear strain timeseries for gauge one, for example. We then calculate the peak value of the RMS strain timeseries, $\hat{\epsilon}$, after applying a two-pass Butterworth highpass filter with a corner frequency of 0.004 Hz (250 s period) to mask out all non-seismic signals that strainmeters have well-known sensitivies to (e.g., tides, atmospheric pressure, etc.); this is the peak dynamic strain (PDS).

Following *Hill* [2008], we estimate peak dynamic stress ($\hat{s}$) as the observed peak RMS strain scaled by twice the crustal shear modulus $\mu$ ($\hat{s} = 2\mu\hat{\epsilon}$). We use $\mu = 30 \times 10^9$ Pa to be consistent with the crustal velocity and density model used to locate the VLFEs. This is a simplistic estimate of the true stresse perturbation, which might be larger if the event occurred where material properties contrast strongly; however, at Cascadia, contrasts in S-wave velocity ($V_S$) at the slab interface are generally within a few percent [*Porritt et al.*, 2011], which translates to a smaller perturbation in $\mu$, given that $\mu = \rho V_S^2$, where $\rho$ is density.

#### *2.3.2 Static Strains from the Local VLFEs*

Theoretically, the lowest detectable static strain is about 0.1–0.2 $\times 10^{-9}$ [parts-per-billion (ppb), or nanostrain]. Following *Wyatt* [1988] this implies that strain from an event with $10^{18}$ N · M seismic moment will be undetectable beyond a few hundred kilometers. However, because of noise and other unrelated signals, the practical limit of detection of an event of this size is ~100–130 km. Relative to the location of VLFE event E3, this limitation leaves 14 possible NOTA stations. However, data from four of these stations are either unavailable or too contaminated with non-seismic signals such that only stations B003, B004, B014, B007, B001, B013, B009, B010, B011, and B926 are useful for analyzing static strains (Figure 7).

The distances from these stations to VLFE event E3 range from 34 to 116 km, which implies that static strains will be much less than 100 ppb [*Wyatt*, 1988]; at these levels, the observed PDS from the 2009 Canal de Ballenas earthquake is at least 3–4 times but possibly 10–100 times larger than the static signal from the VLFE. For this reason, we first detrended the records based on the data seen between the origin time and the first surface-wave arrivals; we then applied a causal, lowpass filter [*Agnew and Hodgkinson*, 2007] to the detrended records to preserve the time-independence of these signals, for comparison with the timing of the VLFEs. Static offsets are computed from these filtered, detrended strain records ($g$), and are then transformed to tensor strain values ($E$) using the coupling equation:

$$E = Cg \tag{1}$$

As described above $g$ is a matrix of strain timeseries from the instrument's 4 strain gauges:

$$g = [g_1, g_2, g_3, g_4]' \tag{2}$$

The matrix $C$ is a 3×4 matrix of calibration coefficients determined by tidal analyses [e.g., *Hodgkinson et al.*, 2013]; it transforms $g$ into tensor strain components and is different for each station. The resulting matrix $E$ contains the areal strain and two engineering shear strains in an east-north (e-n) coordinate reference system, where extensional strains are positive:

$$E = [E_{\mathrm{ee}} + E_{\mathrm{nn}}, E_{\mathrm{ee}} - E_{\mathrm{nn}}, 2E_{\mathrm{en}}]' \tag{3}$$

For instance, the value $E_{\mathrm{ee}}$ represents uniaxial, extension in the east direction. Thus, the rms extension is found through the quadrature sum of the components of $0.5E$, or $E_{\mathrm{RMS}} = \sqrt{(E_{\mathrm{ee}}^2 + E_{\mathrm{nn}}^2 + E_{\mathrm{en}}^2)/3}$, and similarly the shear components of $0.5E$ give the maximum shear strain: $\tau_{\max} = \sqrt{(E_{\mathrm{ee}} - E_{\mathrm{nn}})^2/4 + E_{\mathrm{en}}^2}$. The calibration matrices ($C$) used for these strainmeters are from *Roeloffs* [2010] and *Hodgkinson et al.* [2013] as detailed in Table S3.

## 3 Results

In Cascadia, we detect three new seismic sources that are likely VLFEs (Figure 2). These sources generated coherent, transcontinental wavefields, and were detected by our surface wave detector [*de Groot-Hedlin and Hedlin*, 2015; *Fan et al.*, 2018]. With the measured centroid times and surface-wave propagation directions, we identify three seismic sources offshore Cascadia, E1–E3 (Figure 2). The VLFEs coincide with surface wave arrivals of the 3 August 2009 Mw 6.9 Canal de Ballenas earthquake. The 2009 Mw 6.9 Canal de Ballenas earthquake was a strike-slip event in the north-central region of the Gulf of California, Mexico [*Castro et al.*, 2011]. The earthquake ruptured a segment of an *en echelon* transform fault system with a shallow hypocenter close to the seafloor [*Castro et al.*, 2011; *Plattner et al.*, 2015]. The Canal de Ballenas earthquake generated strong Rayleigh waves, and the observed dynamic strains at NOTA stations were between 2.1 and 15.3 (mean 7.3) times larger than those of most Mw 6.9 teleseisms, according to the relationships of *Agnew and Wyatt* [2014].

The best resolved event (E3) occurred at 18:13:10 UTC, ~764 seconds after the Canal de Ballenas earthquake origin time; its epicenter is near the entrance of the Strait of Juan de Fuca, ~2360 km away from earthquake epicenter (Figure 1). Its coherent waveforms can be clearly identified from the aligned traces (Figure 3). All of the VLFE events

(E1–E3) occurred immediately after the passing seismic waves from the Canal de Ballenas earthquake, and were most likely dynamically triggered by the earthquake. We could not analyze seismic data from stations in the near-field confidently because of the near-instantaneous triggering responses: the long lasting coda waves of the Canal de Ballenas earthquake masked signals of E1–E3 at stations in the Pacific Northwest (Figures 3,S1). However, none of the events (E1–E3) produced visible, high-frequency body-wave phases (Figure S1), nor are they listed in standard catalogs, relinquishing the possibility that instead they are regular earthquakes. Therefore, being in the vicinity of the Cascadia slow earthquakes, our newly located sources are most likely VLFEs.

We verify this hypothesis by modeling the E3 focal-mechanism (Figure 4). The waveforms associated with E3 are well-separated from the surface waves of the Canal de Ballenas earthquake in the far-field, permitting such an analysis; the other two VLFEs are too difficult to model due to the poor signal-to-noise ratios of the records (Figure 3). Therefore, we focus our discussions on event E3 in this study and only report the detections of E1 and E2 (Figure 2). The preferred solution suggests that E3 lasted less than 20 s (a point source) and has a mechanism with a strike of 125°, dip of 1°, and rake of -117° at a depth of 15 km (Figure 5).

The focal-mechanism and depth solution suffers from uncertainties because it is based on a catalog, and the teleseismic surface waves used for the analysis were filtered in a narrow period-band (Figure 4). Since the likely depth range for E3 is 15–25 km (Figure 6), it is difficult to determine how the source depth deviates from the plate interface geometry [*Hayes et al.*, 2018]. However, it is worth noting that the E3 depth range is shallower than the ETS rupture depth of 30–50 km [*Bartlow et al.*, 2011]. After resolving the focal-mechanism and the event depth, we use the amplitude ratios between the synthetic waveforms and the observations to estimate the VLFE moment magnitude. The E3 event had a moment magnitude (Mw) of 5.7 ($0.5 \times 10^{18}$ N · M, Figure 4), which is much larger than those of other VLFEs (M2.1–4.1) in the region [*Hutchison and Ghosh*, 2016; *Ide*, 2016].

At multiple stations near E3 we observe static strain offsets after the E3 occurrence (Figure 6). A table of observed offsets can be found in the Supplement. We ruled out the possibility that these are spurious strains [e.g., *Barbour et al.*, 2015] by confirming the absence of static offsets at distant stations in the region with similar dynamic strain amplitudes (Figure 8). We also note that the observed static strains are not apparent until soon after the seismically-determined origin time of E3 (Figure 6). With the source parameters, we model the static strains due to E3 with an edge dislocation in an elastic halfspace [*Okada*, 1985], and compare the model-predictions with observations at nearby strainmeter stations of the NOTA network (Figure 6 and 7). With the exception of station B003, the overall spatial pattern of the observed static strains from the other nine stations is consistent with the synthetic strains. This confirms the event E3 and its source model, suggesting that these strain data represent the first set of direct observations of static crustal deformation associated with a VLFE.

## 4 Discussions

### 4.1 Resolutions and Uncertainties

The detected VLFEs in Cascadia are unlikely to be data artifacts. Their radiated surface waves, particularly from E3, span most of the United States (Figure 2) and the direct geodetic observations conclusively confirm E3 and that the event occurred near the seismically determined location (Figure 6). Further, E3 can be directly identified from aligned waveforms, furthering confirming its location (Figure 3).

In addition to triggered seismic events, heterogeneous subsurface structure can cause a secondary coherence surface wavefield by reflecting or converting the incoming waves

[*Obara and Matsumura*, 2010; *Maeda et al.*, 2014; *Buehler et al.*, 2018; *Yu et al.*, 2017, 2021]. Here we considered the possibility that the detected VLFEs are actually scattered energy from the Canal de Ballenas event seismic waves rather than a unique local source. For example, the observations could have been from S-wave to surface-wave conversions that have been observed from the US west coast [*Buehler et al.*, 2018; *Yu et al.*, 2021]. However, we found that this hypothesis violates the observations in a number of ways. First, if the VLFEs are S-to-Rayleigh wave or P-to-Rayleigh wave scatterers, these seismic sources would occur upon the body wave arrivals. However, the observations show that the detected seismic sources occurred after the surface waves (Figure 3). Second, previous surface-wave reflections from a single scatter would last longer than 200 s [*Obara and Matsumura*, 2010], which contracts to what we observe for the surface waves of E3 in Figure 3 (duration of E3 is less than 20 s). Lastly, if the detected triggered sources are scatterers, structural heterogeneities (scatterers) would cause the same scattering for earthquakes from the same region, and the seismic sources detected by ALEUMA would be located at the same location and the measured propagation directions would be identical after large triggering earthquakes from the same region [*Obara and Matsumura*, 2010]. However, this is inconsistent with our observations (Figure 9). We observe no triggered seismic sources in Cascadia after the 2010 Mw 7.2 El Mayor-Cucapah earthquake, 2012 Mw 7.0 Baja California earthquake, or the 2019 Mw 7.0 Ridgecrest earthquake. These observations falsify the scattering hypothesis and confirm the observed VLFEs, particularly E3.

While there is good spatial agreement between the observed and modeled static strains (Figure 6a) and no apparent influence from peak dynamic strain (Figure 6b), we note that there are significant uncertainties in the strainmeter calibration coefficients in this region owing to non-linear distortions from ocean loading, which make it notoriously difficult to accurately model tidal strains, which are needed for calibration [see *Hodgkinson et al.*, 2013; *Kamigaichi et al.*, 2021]. We attribute the relatively small strains at B003 to this effect, but also to variations in focal mechanism parameters, which have a strong influence on the spatial pattern of coseismic strain in the near-to-intermediate field, layered structure notwithstanding. Indeed, some stations located between lobes of significant deformation (e.g., Figure 6a) where small changes in strike or dip would have the strongest effect. Unfortunately, there are too few strainmeters near E3 to perform an independent source inversion; but, the current set of static strain observations can conclusively confirm the E3 occurrence and its relatively large moment magnitude. Instead, to independently test the location of E3, we forward modeled the same focal mechanism at every point on the Slab2 subduction zone interface [*Hayes et al.*, 2018] and calculated the source likelihood from the strain data misfit. Owing to station coverage there is a relatively broad zone of plausible source location, but this zone encompasses the seismically-derived location for E3 and the most likely location based on strain observations alone is within tens of km of the seismic location (Figure 7b).

We also compared the timing of the surface waves and VLFE detections with long-term strain records in Cascadia and the detected tremor events from the World Tremor Database (WTD)[*Idehara et al.*, 2014] in Figure 8. These data cannot definitively rule out deformation signals related to slow slip occurring prior to 2009/8/3, but they do show that if slow slip related to the 2009 ETS event initiated before these arrivals, the strain signals are undetectable relative to the non-tectonic noise seen at these stations. Further, the tremor rate increases roughly 10 hours after the triggered VLFE events, as the ETS event is apparently developing; this is juxtaposed by a multi-day quiescence and a lack of slip-related signals in GNSS data prior to the passing seismic waves (Figure 8c).

### 4.2 Triggering and Interaction

Slow earthquakes interact and trigger each other frequently [*Obara and Kato*, 2016]. For example, slow slip events can drive tremor, causing ETS events in Cascadia [*Rogers* *and Dragert*, 2003; *Bartlow et al.*, 2011], and VLFEs have been triggered by long-term SSEs offshore Japan [*Hirose et al.*, 2010; *Araki et al.*, 2017; *Katakami et al.*, 2020]. The close spatiotemporal correlation between the observed VLFEs and the 2009 ETS event in Cascadia suggests that they are likely physically related [*Rubinstein et al.*, 2009]. One possibility is that these large-magnitude VLFEs, caused by the passing seismic waves, may have initiated slow slip event which eventually developed into the 2009 Cascadia ETS event. Presently, we cannot confirm this cascading process, as neither GNSS stations or borehole strainmeters in Cascadia detected slow slips before the 2009 ETS event above background noise levels (Figure 8). Intriguingly, those same geodetic data show no evidence of ETS-related deformation prior to the passing seismic waves, especially in the GNSS displacement records where the ETS-related deformation is most apparent [*Bartlow et al.*, 2011] (Figure 8). Despite the ambiguity in the timing of the 2009 ETS event relative to the VLFEs, our observations suggest that intricate, complex slip interactions may occur more frequently at Cascadia than previously documented.

Slow earthquakes can be susceptible to triggering due to small external stress perturbations [*Obara and Kato*, 2016; *Katakami et al.*, 2020; *Araki et al.*, 2017], which is best illustrated by the sensitivity of tremor occurrence to Earth tides and passing seismic waves [*Rubinstein et al.*, 2008, 2009; *Hawthorne and Rubin*, 2010; *Chao et al.*, 2013; *Houston*, 2015; *Miyazawa*, 2019]. For example, remote triggering of VLFEs by surface waves from a moderate to large, distant earthquake has been reported in the Nankai subduction zone [*Miyazawa*, 2019]. Passing seismic waves also triggered aseismic slip events on the San Andreas fault that led to migrating tremor [*Shelly et al.*, 2011]. Such dynamically triggered cascading slip events may be similar to what we observe in this study. With direct measurements of dynamic strain, we estimate the dynamic stresses associated with the passing seismic waves. Assuming a shear modulus of 30 GPa, the dynamic, elastic stress perturbation from the Canal de Ballenas earthquake was likely 20–30 kPa at E3. The true triggering stresses at E3 could vary within a few percent depending on the depth dependence of surface waves, fault geometry, fault frictional properties, and dynamic pore pressure effects.

The observed triggering process suggests that the E3 patch in the fault gap was at a critical state prior to the surface wave arrivals. Alternatively, the fault could have been very weak, such that the dynamic stress changes from the Canal de Ballenas earthquake were sufficient to trigger an unstable dynamic rupture; in that case, triggered VLFEs would be a commonly-observed phenomenon despite of rare reports for such cases [*Miyazawa*, 2019]. Nonetheless, in this study, the observed VLFEs show that in between the seismogenic zone and the ETS zone, the megathrust fault gap is capable of hosting M5.7 seismic events that are sensitive to transient stress perturbations.

### 4.3 Physical Conditions in Between the Seismogenic and Tremor Zones

Event E3 occurred at depths shallower than other slow earthquakes in the Cascadia subduction zone [*Gomberg et al.*, 2010; *Brudzinski and Allen*, 2007]. Interestingly, neither tremor nor slow slip signals were detected in the region during these triggered VLFEs [*Wech and Creager*, 2008; *Bartlow et al.*, 2011]; this behavior differs from typical VLFEs in this region that are often coincident with tremor and slow slip [*Hutchison and Ghosh*, 2016; *Ide*, 2016]. The relatively shallow depth of E3 corresponds to the deepest part of the locked zone – a gap in between the seismogenic zone and the ETS zone [*Hyndman and Wang*, 1995; *Wang et al.*, 2003; *Priest et al.*, 2010; *Schmalzle et al.*, 2014; *Bruhat and Segall*, 2016]. In northern Cascadia, slow slip events have penetrated upward into this gap zone during previous ETS events, but tremor has been scarce there [*Wang et al.*, 2008; *Wech et al.*, 2009; *Hall et al.*, 2018]. Further, sporadic weak slips are observed in this gap zone across all of Cascadia [*Bartlow*, 2020; *Nuyen and Schmidt*, 2021].

Given the magnitude and location of E3, our observed VLFEs may relate to these aseismic slips, and in combination, their slip contributions may be analogous to the longer-term SSEs in Nankai [*Hirose et al.*, 2010; *Kobayashi*, 2014]. However, the occurrence of E3 also suggests that this gap region is not creeping steadily or slipping aseismically [*Holtkamp and Brudzinski*, 2010; *Hyndman*, 2013; *Schmalzle et al.*, 2014]. Instead, the gap zone is likely partially locked and rupture can propagate sufficiently fast there: estimates of the downdip rupture limit of large megathrust earthquakes may need to be extended [*Ramos and Huang*, 2019]. The observation also indicates that the fault's strength may increase in the gap zone, compared to the ETS zone, suggesting that loading stresses from the ETS events fail to generate seismic failures during conventional Cascadia ETS events, possibly due to the size of the locked fault patch [*Hall et al.*, 2018]. Conceptually, the gap zone may be comprised of large strong fault patches that can generate VLFEs [*Chestler and Creager*, 2017], surrounded by a ductile matrix that could slip aseismically as previous ETS events have shown [*Wang et al.*, 2008; *Hall et al.*, 2018]. Such cases may explain our observed VLFEs with a lack of tremor activity in the gap zone, presumably related to the nonstationary shear stress rates inferred from decadally-averaged crustal deformation rates [*Bruhat and Segall*, 2016]. Our observations warn that future megathrust earthquakes could penetrate beyond the locking depth (~20 km) at some parts of the subduction zone and generate intense ground shaking along the densely populated margin [*Melgar et al.*, 2016; *Frankel et al.*, 2018; *Wirth et al.*, 2018; *Ramos and Huang*, 2019].

### 4.4 Breakdown of the Slow Earthquake Scaling Relationship?

It has been suggested that slow earthquakes, including VLFEs, follow an apparent moment-duration scaling relationship where the moment rate of these events is likely constant and the final seismic moment is proportional to the characteristic duration [*Ide et al.*, 2007]. This would be different from the scaling of regular earthquakes, for which moment scales linearly with the cube of the characteristic duration [*Houston*, 2001]. Further, slow earthquakes are thought to rupture faster than the plate movement rate, but their rupture speeds cannot accelerate to those of typical earthquakes [*Gao et al.*, 2012; *Bletery et al.*, 2017]. If those empirical scaling relationships hold true, we would expect a M5.7 VLFE or slow earthquake to last from 6 days to a month [*Ide et al.*, 2007]. Consequentially, the rupture speed of such an event would be too slow to generate seismic signals that can be observed in the far field [*Gao et al.*, 2012]. Here, seismic and geodetic observations directly refute such slow earthquake scaling relationships: waveform modeling shows that E3 was likely a transient event, which duration is much less than the predicted duration from the slow earthquake scaling relationship (Figure 4) but is in closer agreement with the scaling of regular earthquakes [*Houston*, 2001] and static strains developed within the duration timescale (Figure 6). Still, event E3 is not a typical earthquake as no high-frequency seismic radiation was observed at seismic stations in the Pacific Northwest (Figure S1). Our reported VLFEs seem to be distinct from other Cascadia VLFEs or slow earthquakes in Nankai [*Ghosh et al.*, 2015; *Hutchison and Ghosh*, 2016; *Obara and Kato*, 2016; *Ide et al.*, 2007]. Our findings raise new questions about the physical nature of the gap zone: is there a new class of slip events that represents a bridge between future megathrust earthquakes and ETS events in Cascadia?

## 5 Conclusions

Ever since the discovery of the ETS events, the nature of the fault area in between the ETS and seismogenic zones in Cascadia has been argued about. By analyzing continuous data from seismic stations across the United States, we identify and locate 3 previously unknown VLFEs that are close to the slip area of the 2009 Cascadia ETS event and occurred three days before the initiation of ETS tremor activity. Particularly, we discover one VLFE located in the critical gap zone with a moment magnitude of 5.7; this is the largest VLFE that has ever been identified across all subduction zones. Further, this is the first time that a VLFE is recorded geodetically, with an array of strainmeters showing clear deformation signals associated with the event. Our findings suggest that the gap zone is capable of hosting large, fast slip events, indicating possible down-dip extension of future megathrust earthquakes in Cascadia. Our observed VLFEs also show that the Cascadia megathrust is weak and is sensitive to transient stress perturbations. Lastly, the identified VLFEs challenge the current understanding of slow earthquake physics, with characteristics that deviate away from the empirical scaling relations of slow earthquakes.

## Open Research

The seismic data were provided by Data Management Center (DMC) of the Incorporated Research Institutions for Seismology (IRIS). The facilities of IRIS Data Services, and specifically the IRIS Data Management Center, were used for access to waveforms, related metadata, and/or derived products used in this study. IRIS Data Services are funded through the Seismological Facilities for the Advancement of Geoscience and EarthScope (SAGE) Proposal of the National Science Foundation (NSF) under Cooperative Agreement EAR-1261681. High-frequency strain data from the Network of the Americas (NOTA) network were also obtained from the IRIS DMC; this material is based on services provided by the Geodesy Advancing Geosciences and EarthScope (GAGE) facility, operated by UNAVCO, Inc., with support from the NSF and the National Aeronautics and Space Administration (NASA) under NSF Cooperative Agreement EAR-1724794. NOTA Level 2 strain and GNSS data were obtained from UNAVCO web-services (`https://www.unavco.org/data/web-services/web-services.html`). The tremor catalog is obtained from the Pacific Northwest Seismic Network and the World Tremor Database (`http://www-solid.eps.s.u-tokyo.ac.jp/~idehara/wtd0/Welcome.html`). The earthquake catalogs used in this study are from the Global Centroid Moment Tensor project (GCMT) *Ekström et al.* [2012].

**Acknowledgments**

We thank David Shelly and Joan Gomberg for constructive comments that led to significant improvements to this manuscript. W.F. was supported by NSF EAR-2022441. Any use of trade, firm, or product names is for descriptive purposes only and does not imply endorsement by the U.S. government.

## References

Agnew, D. C., and K. Hodgkinson (2007), Designing compact causal digital filters for low-frequency strainmeter data, *Bulletin of the Seismological Society of America*, *97*(1B), 91–99, doi:10.1785/0120060088.

Agnew, D. C., and F. K. Wyatt (2014), Dynamic strains at regional and teleseismic distances, *Bulletin of the Seismological Society of America*, *104*(4), 1846–1859, doi:10.1785/0120140007.

Araki, E., D. M. Saffer, A. J. Kopf, L. M. Wallace, T. Kimura, Y. Machida, S. Ide, E. Davis, and (2017), Recurring and triggered slow-slip events near the trench at the Nankai Trough subduction megathrust, *Science*, *356*(6343), 1157–1160, doi:10.1126/science.aan3120.

Barbour, A. J., and B. W. Crowell (2017), Dynamic strains for earthquake source characterization, *Seismological Research Letters*, *88*(2A), 354–370.

Barbour, A. J., D. C. Agnew, and F. K. Wyatt (2015), Coseismic Strains on Plate Boundary Observatory Borehole Strainmeters in Southern California, *Bulletin of the Seismological Society of America*, *105*(1), 431–444, doi:10.1785/0120140199.

Bartlow, N. M. (2020), A long-term view of episodic tremor and slip in Cascadia, *Geophysical Research Letters*, *47*(3), e2019GL085,303.

Bartlow, N. M., S. Miyazaki, A. M. Bradley, and P. Segall (2011), Space-time correlation of slip and tremor during the 2009 Cascadia slow slip event, *Geophysical Research Letters*, *38*(18).

Bletery, Q., A. M. Thomas, J. C. Hawthorne, R. M. Skarbek, A. W. Rempel, and R. D. Krogstad (2017), Characteristics of secondary slip fronts associated with slow earthquakes in Cascadia, *Earth and Planetary Science Letters*, *463*, 212–220.

Bostock, M., A. Royer, E. Hearn, and S. Peacock (2012), Low frequency earthquakes below southern Vancouver Island, *Geochemistry, Geophysics, Geosystems*, *13*(11).

Brown, J. R., G. C. Beroza, S. Ide, K. Ohta, D. R. Shelly, S. Y. Schwartz, W. Rabbel, M. Thorwart, and H. Kao (2009), Deep low-frequency earthquakes in tremor localize to the plate interface in multiple subduction zones, *Geophysical Research Letters*, *36*(19).

Brudzinski, M. R., and R. M. Allen (2007), Segmentation in episodic tremor and slip all along Cascadia, *Geology*, *35*(10), 907–910.

Bruhat, L., and P. Segall (2016), Coupling on the northern Cascadia subduction zone from geodetic measurements and physics-based models, *Journal of Geophysical Research: Solid Earth*, *121*(11), 8297–8314.

Buehler, J., N. Mancinelli, and P. Shearer (2018), S-to-Rayleigh Wave Scattering From the Continental Margin Observed at USArray, *Geophysical Research Letters*, *45*(10), 4719–4724.

Castro, R. R., C. Valdés-González, P. Shearer, V. Wong, L. Astiz, F. Vernon, A. Pérez-Vertti, and A. Mendoza (2011), The 3 August 2009 Mw 6.9 Canal de Ballenas region, Gulf of California, earthquake and its aftershocks, *Bulletin of the Seismological Society of America*, *101*(3), 929–939.

Chao, K., Z. Peng, H. Gonzalez-Huizar, C. Aiken, B. Enescu, H. Kao, A. A. Velasco, K. Obara, and T. Matsuzawa (2013), A Global search for triggered tremor following the 2011 Mw 9.0 Tohoku earthquake, *Bulletin of the Seismological Society of America*, *103*(2 B), 1551–1571, doi:10.1785/0120120171.

Chestler, S., and K. Creager (2017), A model for low-frequency earthquake slip, *Geochemistry, Geophysics, Geosystems*, *18*(12), 4690–4708.

de Groot-Hedlin, C. D., and M. A. Hedlin (2015), A method for detecting and locating geophysical events using groups of arrays, *Geophysical Journal International*, *203*(2), 960–971.

Dragert, H., K. Wang, and T. S. James (2001), A silent slip event on the deeper Cascadia subduction interface, *Science*, *292*(5521), 1525–1528.

Driel, M. v., L. Krischer, S. C. Stähler, K. Hosseini, and T. Nissen-Meyer (2015), Instaseis: Instant global seismograms based on a broadband waveform database, *Solid Earth*, (2), 701–717.

Dziewonski, A. M., and D. L. Anderson (1981), Preliminary reference Earth model, *Physics of the earth and planetary interiors*, *25*(4), 297–356.

Ekström, G., M. Nettles, and A. Dziewoński (2012), The global CMT project 2004–2010: Centroid-moment tensors for 13,017 earthquakes, *Physics of the Earth and Planetary Interiors*, *200*, 1–9.

Fan, W., C. D. de Groot-Hedlin, M. A. Hedlin, and Z. Ma (2018), Using surface waves recorded by a large mesh of three-element arrays to detect and locate disparate seismic sources, *Geophysical Journal International*, *215*(2), 942–958.

Fan, W., J. J. McGuire, C. D. de Groot-Hedlin, M. A. Hedlin, S. Coats, and J. W. Fiedler (2019), Stormquakes, *Geophysical Research Letters*, *46*(22), 12,909–12,918.

Fan, W., J. J. McGuire, and P. M. Shearer (2020), Abundant spontaneous and dynamically triggered submarine landslides in the Gulf of Mexico, *Geophysical Research Letters*, *47*(12), e2020GL087,213.

Frankel, A., E. Wirth, N. Marafi, J. Vidale, and W. Stephenson (2018), Broadband synthetic seismograms for magnitude 9 earthquakes on the Cascadia megathrust based on 3D simulations and stochastic synthetics, Part 1: Methodology and overall results, *Bulletin of the Seismological Society of America*, *108*(5A), 2347–2369.

Gao, H., D. A. Schmidt, and R. J. Weldon (2012), Scaling relationships of source parameters for slow slip events, *Bulletin of the Seismological Society of America*, *102*(1), 352–360.

Ghosh, A., E. Huesca-Pérez, E. Brodsky, and Y. Ito (2015), Very low frequency earthquakes in Cascadia migrate with tremor, *Geophysical Research Letters*, *42*(9), 3228–3232.

Gladwin, M. T. (1984), High-precision multicomponent borehole deformation monitoring, *Review of Scientific Instruments*, *55*(12), 2011–2016, doi:10.1063/1.1137704.

Gomberg, J., C. 2007, and the Cascadia 2007 and Beyond Working Group (2010), Slow-slip phenomena in Cascadia from 2007 and beyond: A review, *GSA Bulletin*, *122*(7-8), 963–978.

Hall, K., H. Houston, and D. Schmidt (2018), Spatial comparisons of tremor and slow slip as a constraint on fault strength in the northern Cascadia subduction zone, *Geochemistry, Geophysics, Geosystems*, *19*(8), 2706–2718.

Hawthorne, J. C., and A. M. Rubin (2010), Tidal modulation of slow slip in Cascadia, *Journal of Geophysical Research: Solid Earth*, *115*(B9).

Hayes, G. P., G. L. Moore, D. E. Portner, M. Hearne, H. Flamme, M. Furtney, and G. M. Smoczyk (2018), Slab2, a comprehensive subduction zone geometry model, *Science*, *362*(6410), 58–61.

Hill, D. P. (2008), Dynamic stresses, Coulomb failure, and remote triggering, *Bulletin of the Seismological Society of America*, *98*(1), 66–92.

Hirose, H., Y. Asano, K. Obara, T. Kimura, T. Matsuzawa, S. Tanaka, and T. Maeda (2010), Slow earthquakes linked along dip in the Nankai subduction zone, *Science*, *330*(6010), 1502–1502.

Hodgkinson, K., J. Langbein, B. Henderson, D. Mencin, and A. Borsa (2013), Tidal calibration of plate boundary observatory borehole strainmeters, *Journal of Geophysical Research: Solid Earth*, *118*(1), 447–458, doi:10.1029/2012jb009651.

Holtkamp, S., and M. R. Brudzinski (2010), Determination of slow slip episodes and strain accumulation along the Cascadia margin, *Journal of Geophysical Research: Solid Earth*, *115*(B4).

Houston, H. (2001), Influence of depth, focal mechanism, and tectonic setting on the shape and duration of earthquake source time functions, *Journal of Geophysical Research: Solid Earth*, *106*(B6), 11,137–11,150.

Houston, H. (2015), Low friction and fault weakening revealed by rising sensitivity of tremor to tidal stress, *Nature Geoscience*, *8*(5), 409–415.

Hutchison, A. A., and A. Ghosh (2016), Very low frequency earthquakes spatiotemporally asynchronous with strong tremor during the 2014 episodic tremor and slip event in Cascadia, *Geophysical Research Letters*, *43*(13), 6876–6882.

Hyndman, R., and K. Wang (1995), The rupture zone of Cascadia great earthquakes from current deformation and the thermal regime, *Journal of Geophysical Research: Solid Earth*, *100*(B11), 22,133–22,154.

Hyndman, R. D. (2013), Downdip landward limit of Cascadia great earthquake rupture, *Journal of Geophysical Research: Solid Earth*, *118*(10), 5530–5549.

Ide, S. (2016), Characteristics of slow earthquakes in the very low frequency band: Application to the Cascadia subduction zone, *Journal of Geophysical Research: Solid Earth*, *121*(8), 5942–5952.

Ide, S., G. C. Beroza, D. R. Shelly, and T. Uchide (2007), A scaling law for slow earthquakes, *Nature*, *447*(7140), 76–79.

Idehara, K., S. Yabe, and S. Ide (2014), Regional and global variations in the temporal clustering of tectonic tremor activity, *Earth, Planets and Space*, *66*(1), 1–10, doi:10.1186/1880-5981-66-66.

Ito, Y., and K. Obara (2006), Dynamic deformation of the accretionary prism excites very low frequency earthquakes, *Geophysical Research Letters*, *33*(2).

Kamigaichi, O., N. Matsumoto, and F. Hirose (2021), Green's function at depth of borehole observation required for precise estimation of the effect of ocean tidal loading near coasts, *Geophysical Journal International*, doi:10.1093/gji/ggab216, ggab216.

Kao, H., K. Wang, H. Dragert, J. Y. Kao, and G. Rogers (2010), Estimating seismic moment magnitude (Mw) of tremor bursts in northern Cascadia: Implications for the seismic efficiency of episodic tremor and slip, *Geophysical Research Letters*, *37*(19).

Katakami, S., Y. Kaneko, Y. Ito, and E. Araki (2020), Stress Sensitivity of Instantaneous Dynamic Triggering of Shallow Slow Slip Events, *Journal of Geophysical Research: Solid Earth*, *125*(6), e2019JB019,178, doi:https://doi.org/10.1029/2019JB019178, e2019JB019178 2019JB019178.

Kobayashi, A. (2014), A long-term slow slip event from 1996 to 1997 in the Kii Channel, Japan, *Earth, Planets and Space*, *66*(1), 1–7.

Maeda, T., T. Furumura, and K. Obara (2014), Scattering of teleseismic P-waves by the Japan Trench: A significant effect of reverberation in the seawater column, *Earth and Planetary Science Letters*, *397*, 101–110.

Melgar, D., R. J. LeVeque, D. S. Dreger, and R. M. Allen (2016), Kinematic rupture scenarios and synthetic displacement data: An example application to the Cascadia subduction zone, *Journal of Geophysical Research: Solid Earth*, *121*(9), 6658–6674.

Miyazawa, M. (2019), Bayesian approach for detecting dynamically triggered very low-frequency earthquakes in the Nankai subduction zone and application to the 2016 Mw 5.9 off-Kii Peninsula earthquake, Japan, *Geophysical Journal International*, *217*(2), 1123–1140.

Nissen-Meyer, T., M. v. Driel, S. Stähler, K. Hosseini, S. Hempel, L. Auer, A. Colombi, and A. Fournier (2014), AxiSEM: broadband 3-D seismic wavefields in axisymmetric media, *Solid Earth*, (1), 425–445.

Nuyen, C. P., and D. A. Schmidt (2021), Filling the Gap in Cascadia: The Emergence of Low-Amplitude Long-Term Slow Slip, *Geochemistry, Geophysics, Geosystems*, *22*(3), e2020GC009,477.

Obara, K., and A. Kato (2016), Connecting slow earthquakes to huge earthquakes, *Science*, *353*(6296), 253–257, doi:10.1126/science.aaf1512.

Obara, K., and M. Matsumura (2010), Reverse propagation of surface waves reflected from seamounts in the Northwestern Pacific, *Bulletin of the Seismological Society of America*, *100*(3), 1342–1349.

Okada, Y. (1985), Surface deformation due to shear and tensile faults in a half-space, *Bulletin of the seismological society of America*, *75*(4), 1135–1154.

Peng, Z., and J. Gomberg (2010), An integrated perspective of the continuum between earthquakes and slow-slip phenomena, *Nature geoscience*, *3*(9), 599–607.

Plattner, C., R. Malservisi, F. Amelung, T. H. Dixon, M. Hackl, A. Verdecchia, P. Lonsdale, F. Suarez-Vidal, and J. Gonzalez-Garcia (2015), Space geodetic observation of the deformation cycle across the Ballenas Transform, Gulf of California, *Journal of Geophysical Research: Solid Earth*, *120*(8), 5843–5862.

Porritt, R. W., R. M. Allen, D. C. Boyarko, and M. R. Brudzinski (2011), Investigation of Cascadia segmentation with ambient noise tomography, *Earth and Planetary Science Letters*, *309*(1), 67–76, doi:https://doi.org/10.1016/j.epsl.2011.06.026.

Priest, G. R., C. Goldfinger, K. Wang, R. C. Witter, Y. Zhang, and A. M. Baptista (2010), Confidence levels for tsunami-inundation limits in northern Oregon inferred from a 10,000-year history of great earthquakes at the Cascadia subduction zone, *Natural Hazards*, *54*(1), 27–73.

Ramos, M. D., and Y. Huang (2019), How the transition region along the Cascadia megathrust influences coseismic behavior: Insights from 2-D dynamic rupture simulations, *Geophysical Research Letters*, *46*(4), 1973–1983.

Roeloffs, E. (2010), Tidal calibration of Plate Boundary Observatory borehole strainmeters: Roles of vertical and shear coupling, *Journal of Geophysical Research: Solid Earth*, *115*(B6), doi:10.1029/2009JB006407.

Rogers, G., and H. Dragert (2003), Episodic tremor and slip on the Cascadia subduction zone: The chatter of silent slip, *Science*, *300*(5627), 1942–1943.

Rubinstein, J. L., M. La Rocca, J. E. Vidale, K. C. Creager, and A. G. Wech (2008), Tidal modulation of nonvolcanic tremor, *Science*, *319*(5860), 186–189.

Rubinstein, J. L., J. Gomberg, J. E. Vidale, A. G. Wech, H. Kao, K. C. Creager, and G. Rogers (2009), Seismic wave triggering of nonvolcanic tremor, episodic tremor and slip, and earthquakes on Vancouver Island, *Journal of Geophysical Research: Solid Earth*, *114*(B2).

Schmalzle, G. M., R. McCaffrey, and K. C. Creager (2014), Central Cascadia subduction zone creep, *Geochemistry, Geophysics, Geosystems*, *15*(4), 1515–1532.

Shelly, D. R., Z. Peng, D. P. Hill, and C. Aiken (2011), Triggered creep as a possible mechanism for delayed dynamic triggering of tremor and earthquakes, *Nature Geoscience*, *4*(6), 384.

Sweet, J. R., K. C. Creager, H. Houston, and S. R. Chestler (2019), Variations in Cascadia low-frequency earthquake behavior with downdip distance, *Geochemistry, Geophysics, Geosystems*, *20*(2), 1202–1217.

Walton, M. A., L. M. Staisch, T. Dura, J. K. Pearl, B. Sherrod, J. Gomberg, S. Engelhart, A. Tréhu, J. Watt, J. Perkins, et al. (2021), Toward an Integrative Geological and Geophysical View of Cascadia Subduction Zone Earthquakes, *Annual Review of Earth and Planetary Sciences*, *49*.

Wang, K., and A. M. Tréhu (2016), Invited review paper: Some outstanding issues in the study of great megathrust earthquakes: The Cascadia example, *Journal of Geodynamics*, *98*, 1–18.

Wang, K., R. Wells, S. Mazzotti, R. D. Hyndman, and T. Sagiya (2003), A revised dislocation model of interseismic deformation of the Cascadia subduction zone, *Journal of Geophysical Research: Solid Earth*, *108*(B1).

Wang, K., H. Dragert, H. Kao, and E. Roeloffs (2008), Characterizing an uncharacteristic ETS event in northern Cascadia, *Geophysical Research Letters*, *35*(15).

Wech, A. G., and N. M. Bartlow (2014), Slip rate and tremor genesis in Cascadia, *Geophysical Research Letters*, *41*(2), 392–398.

Wech, A. G., and K. C. Creager (2008), Automated detection and location of Cascadia tremor, *Geophysical Research Letters*, *35*(20).

Wech, A. G., K. C. Creager, and T. I. Melbourne (2009), Seismic and geodetic constraints on Cascadia slow slip, *Journal of Geophysical Research: Solid Earth*, *114*(B10).

Wirth, E. A., A. D. Frankel, N. Marafi, J. E. Vidale, and W. J. Stephenson (2018), Broadband synthetic seismograms for magnitude 9 earthquakes on the Cascadia megathrust based on 3D simulations and stochastic synthetics, Part 2: Rupture parameters and variability, *Bulletin of the Seismological Society of America*, *108*(5A), 2370–2388.

Wyatt, F. K. (1988), Measurements of Coseismic Deformation in Southern California: 1972-1982, *J. Geophys. Res.*, *93*(B7), 7923–7942, doi:10.1029/JB093iB07p07923.

Yu, C., Z. Zhan, E. Hauksson, and E. S. Cochran (2017), Strong SH-to-love wave scattering off the Southern California continental borderland, *Geophysical Research Letters*, *44*(20), 10–208.

Yu, C., J. C. Castellanos, and Z. Zhan (2021), Imaging strong lateral heterogeneities across the contiguous US using body-to-surface wave scattering, *Journal of Geophysical Research. Solid Earth*, *126*(1), Art–No.

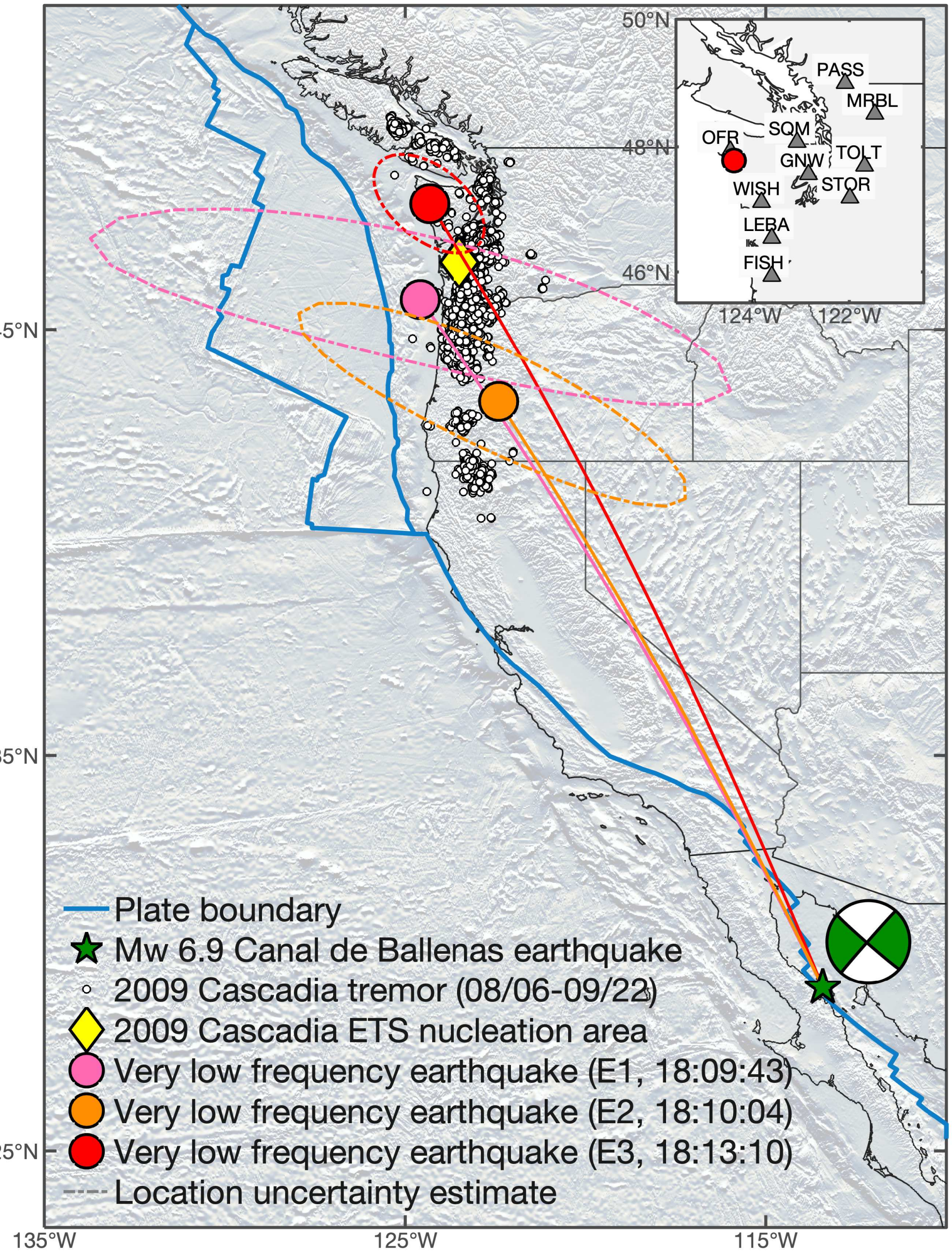


**Figure 1.** The 2009 M6.9 Canal de Ballenas earthquake, the 2009 Cascadia episodic tremor and slip (ETS) event, and three dynamically triggered very low frequency earthquakes (VLFEs, E1–E3). Inset: broadband near-field stations in the Pacific Northwest.

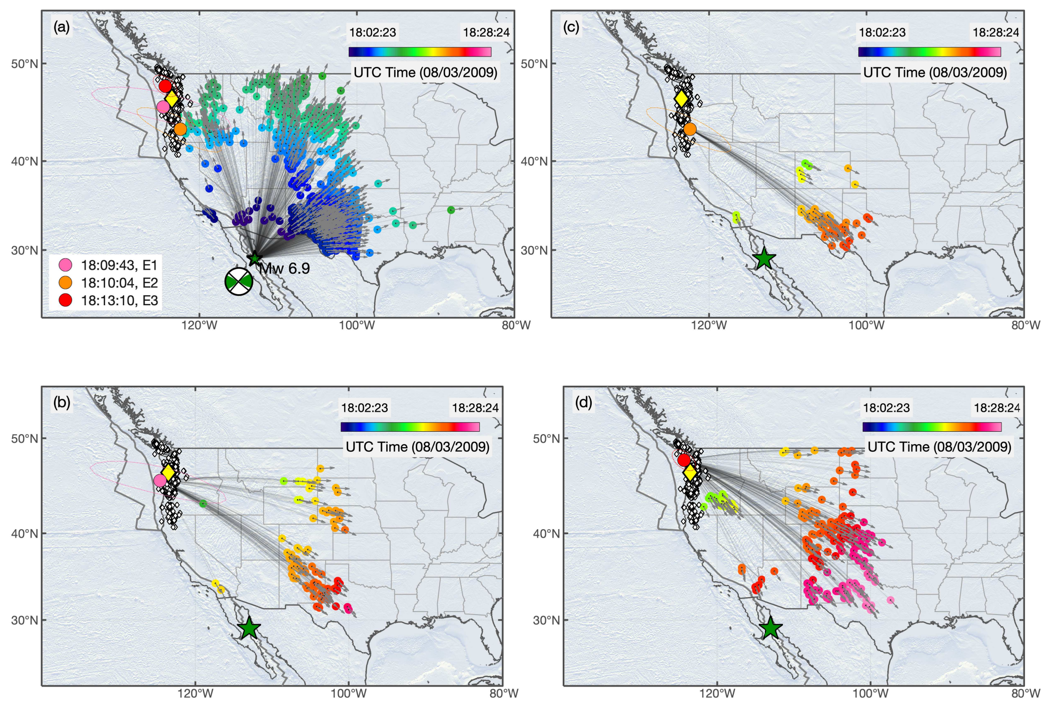


**Figure 2.** The very low frequency earthquakes and the triggering 2009 M6.9 earthquake (a). The legends are similar to those of Figure 1. The Rayleigh wave arrival times and propagation directions are shown as the colored dots and arrows. The thin gray lines show the great circle paths from the source to the subarrays. The four events share the same colorbar. These three VLFEs were detected by 84 (b), 57 (c), and 187 (d) subarrays, respectively.

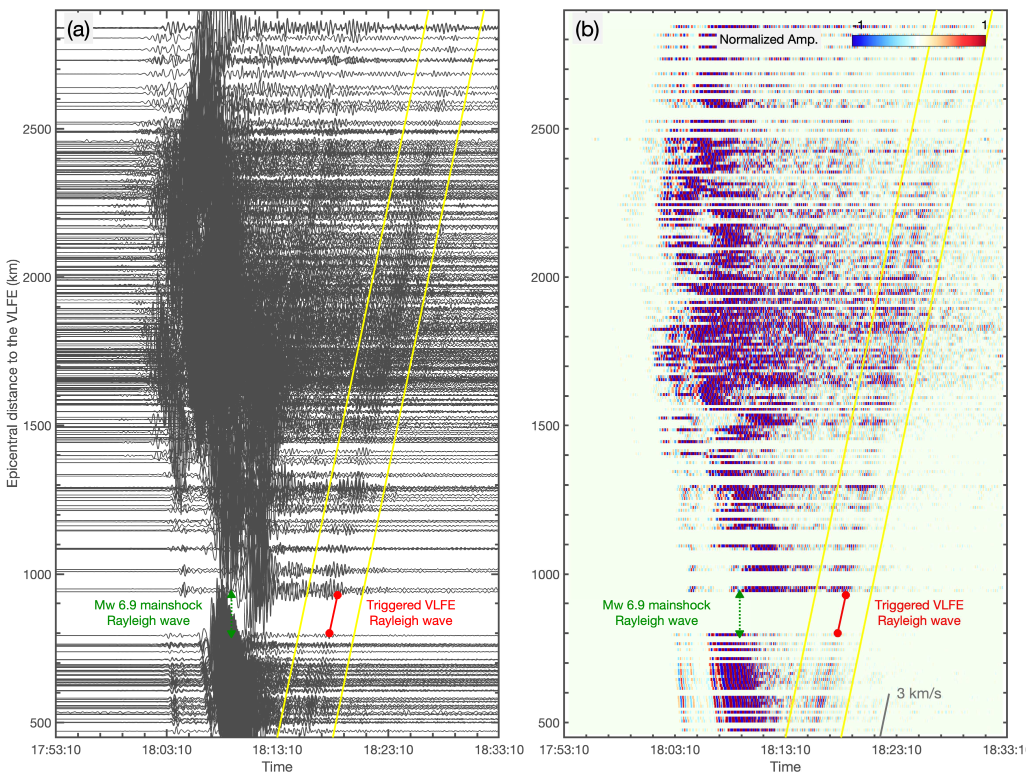


**Figure 3.** Record sections that are aligned with the epicenter of the VLFE E3 in Figure 2d. The records are self-normalized and bandpass-filtered to show signals in the 20–50 s period band. The yellow lines show a 3 km/s reference move-out velocity, windowing the VLFE waveforms. (a), waveform records. (b), polarity plot.

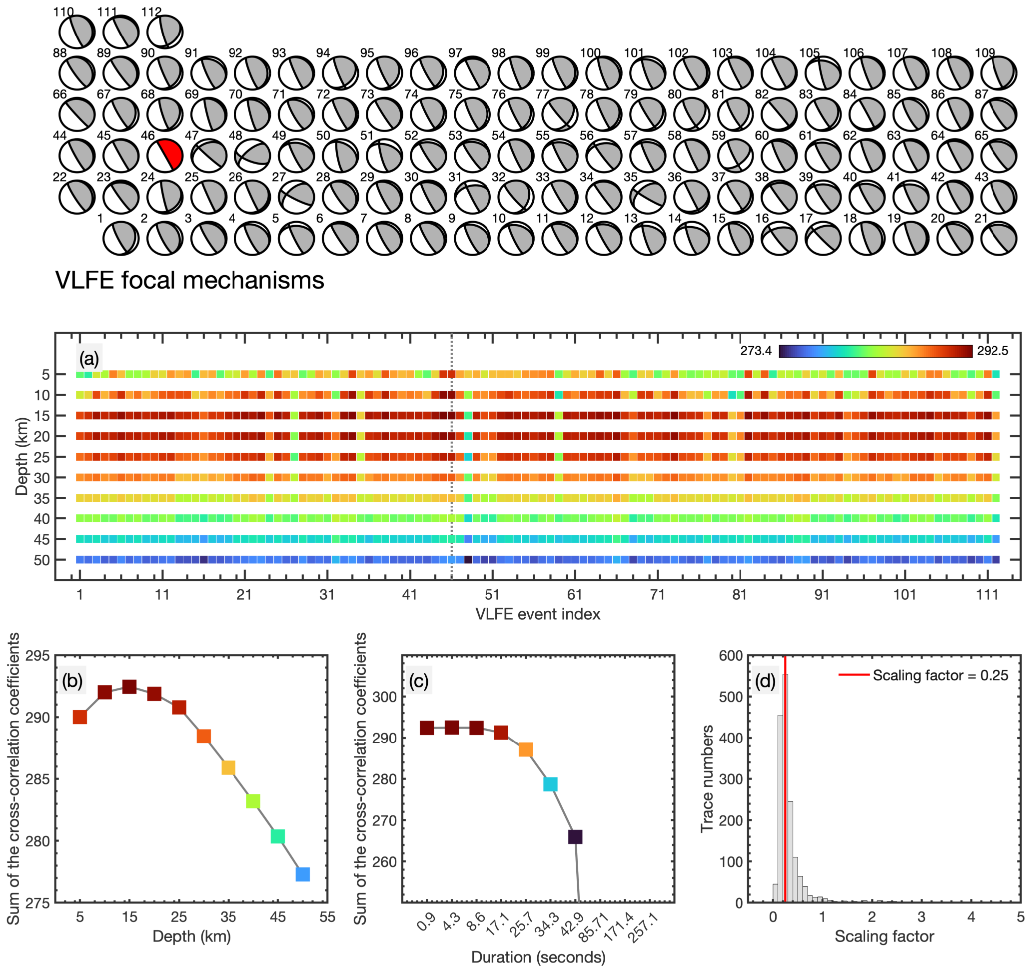


**Figure 4.** Determining the focal-mechanism of VLFE E3. The VLFE focal mechanisms are shown in the top panel with their event index listed at their upper left corner [*Ide*, 2016]. The optimal focal-mechanism is denoted as the red beachball. (a), total cross-correlation coefficients of the 112 candidate focal-mechanisms. The total cross-correlation coefficient for a focal-mechanism is the sum of the average cross-correlation coefficients of all the analyzed stations. (b), VLFE depth of E3 event showing total cross-correlation coefficients for the optimal focal-mechanism at depth from 5 to 50 km (c), VLFE duration of E3 showing total cross-correlation coefficients for the optimal focal-mechanism with duration from 0.9 to 257.1 seconds. We assume a Gaussian function shape with the duration as 6 times the standard deviation.(d) scaling factor of the VLFE moment. The testing moment is $2\times10^{18}$ N $\cdot$ M. With the scaling factor, the VLFE moment is $0.5\times10^{18}$ N $\cdot$ M, equivalent to a moment magnitude of 5.7.

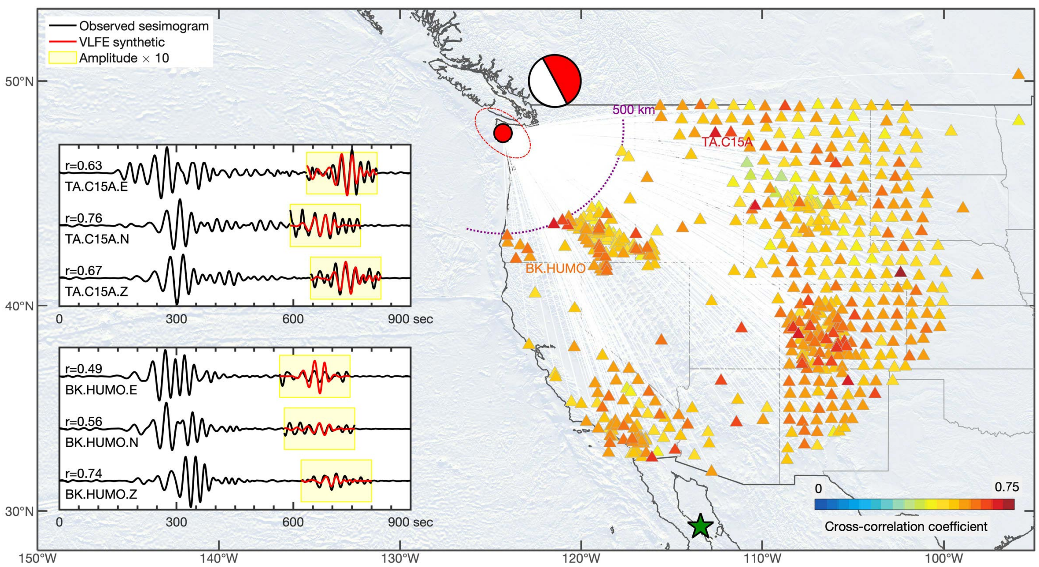


**Figure 5.** Seismic observations of E3 showing the average cross-correlation coefficients of the synthetic and observed waveforms of the VLFE E3. The average cross-correlation coefficient of a station is obtained by geometrically averaging coefficients of the three-component records. Insets: example three-component waveforms of the mainshock and the VLFE, overlain with synthetic waveforms of the VLFE. The two stations are at the eastward and the southward directions of the VLFE, respectively. The yellow shaded regions show records amplified by ten times.

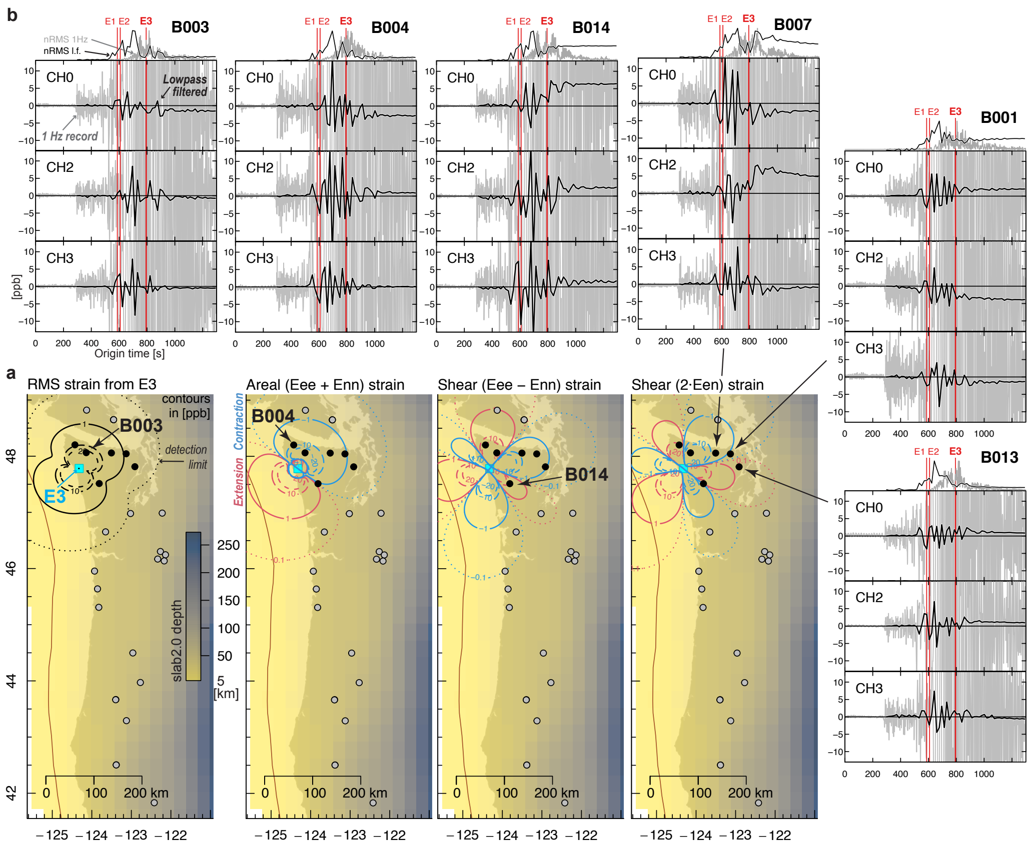


**Figure 6.** Static strains associated with triggered VLFE detection E3. (a) Contours of modeled static deformation from the best fitting focal mechanism for E3, in parts-per-billion (ppb), including root-mean-square (RMS) strain, areal strain ($E_{\mathrm{ee}}$ + $E_{\mathrm{nn}}$), engineering shear strains $E_{\mathrm{ee}}$ - $E_{\mathrm{nn}}$ and $2E_{\mathrm{en}}$. (b) Observations of static strains in high-frequency (1 Hz) strain records from B003, B004, B014, B007, B001, and B013. For each strainmeter channel, we show the lowpass filtered record, obtained with a causal filter with a 18 s corner period (56 mHz), overlain on the original record. Vertical lines show the origin times of the VLFE detections E1–E3: static strains are not apparent until after E3. Self-normalized RMS strain records are shown at the top: E3 occurs around the time of maximum 1 Hz RMS strain, after the peak in low-frequency RMS strain.

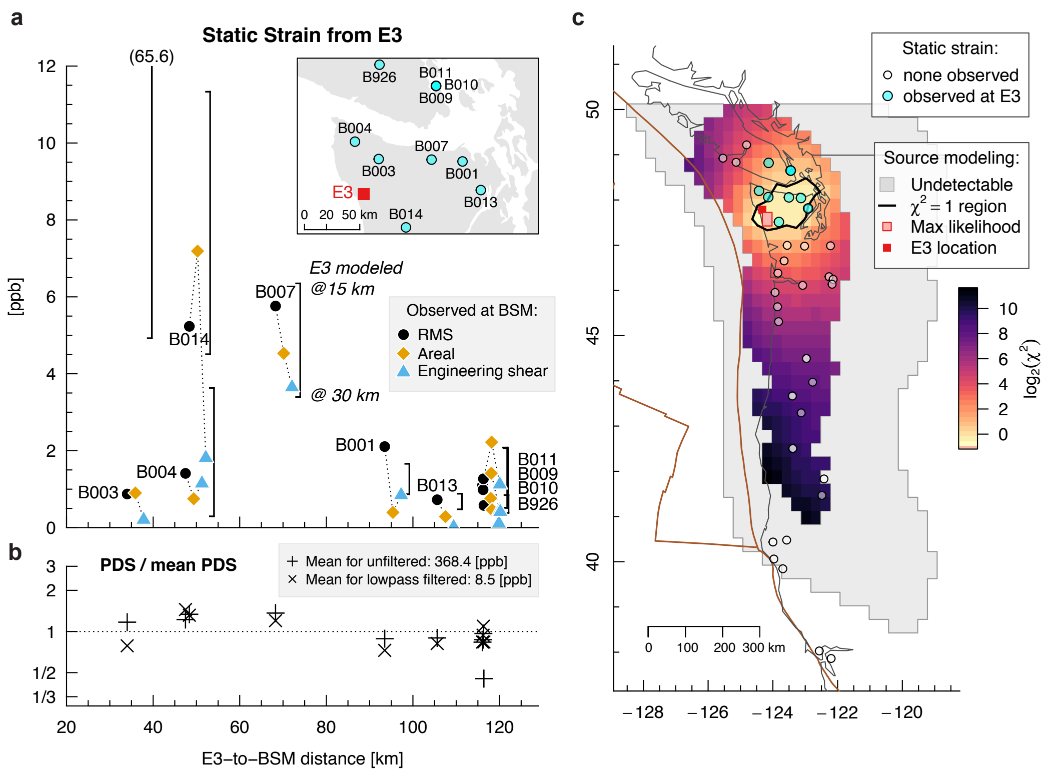


**Figure 7.** Variability in modeled static strains from depth and location uncertainty. (a) Observed tensor strains compared to a range of model results found by varying the source depth from 15 km to 30 km. (b) Peak dynamic strain (PDS) from the teleseimic waves. Points show the ratio of the PDS at each station to the mean value for all stations, for both unfiltered (1 Hz) and lowpassed (56 mHz) records; values are shown on a log scale. As expected, the PDS is relatively consistent across the study region. (c) Map of source likelihood found by moving the E3 source to each point on the Slab2.0 surface, forward modeling the static strains and computing the misfit. Colors show the base-2 logarithm of the reduced Chi-squared misfit ($\chi^2$); the black line shows the region where residual variance is equal to observational variance ($\chi^2 = 1$). The cell with the lowest-misfit, outlined in red, is near the triggered VLFE detection E3.

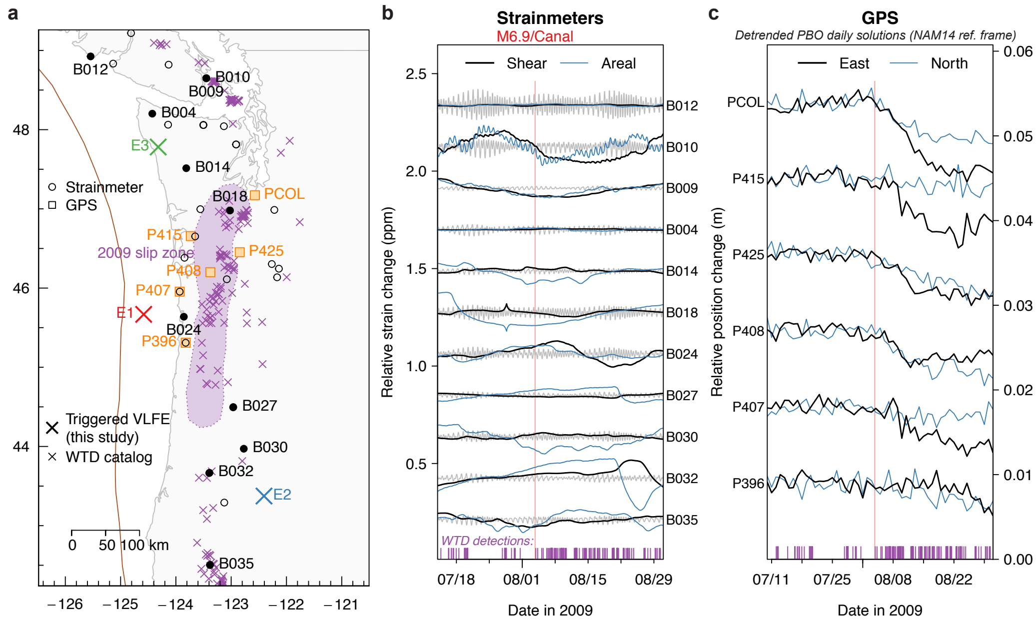


**Figure 8.** Lack of evidence for geodetic deformation in Cascadia prior to seismic arrivals from the 2009/8/3 Canal de Ballenas event seen in borehole strainmeter and GNSS data from 2009/7/12 to 2009/9/1. (a) Map of the NOTA BSM network and selected GNSS stations, VLFE detections from this study (E1–E3), and tremor detections from the World Tremor Database (WTD) [*Idehara et al.*, 2014]. The filled polygon is the region of significant slow slip inferred primarily from these GNSS stations [*Bartlow et al.*, 2011]. (b) Shear and areal strains from NOTA strainmeters, specifically the locations with filled circles in (a). Strains have been corrected for atmospheric pressure and tidal loading (tidal corrections shown in grey), detrended, and lowpass filtered with a causal filter at 2.5 days. Shown below these timeseries is the WTD catalog (see a); the first event on 2009/8/3 occurred at 21:24:14 UTC, approximately 10 hours after events E1–E3. (c) Detrended timeseries of PBO daily position solutions in NAM14 reference frame, at stations shown in (a). Noise levels notwithstanding, the initiation of the 2009 ETS slow slip event appears to coincide with the Canal de Ballenas seismic arrivals; slip is modeled to begin after 8/3 and is clearly developed by the 7th [*Bartlow et al.*, 2011].

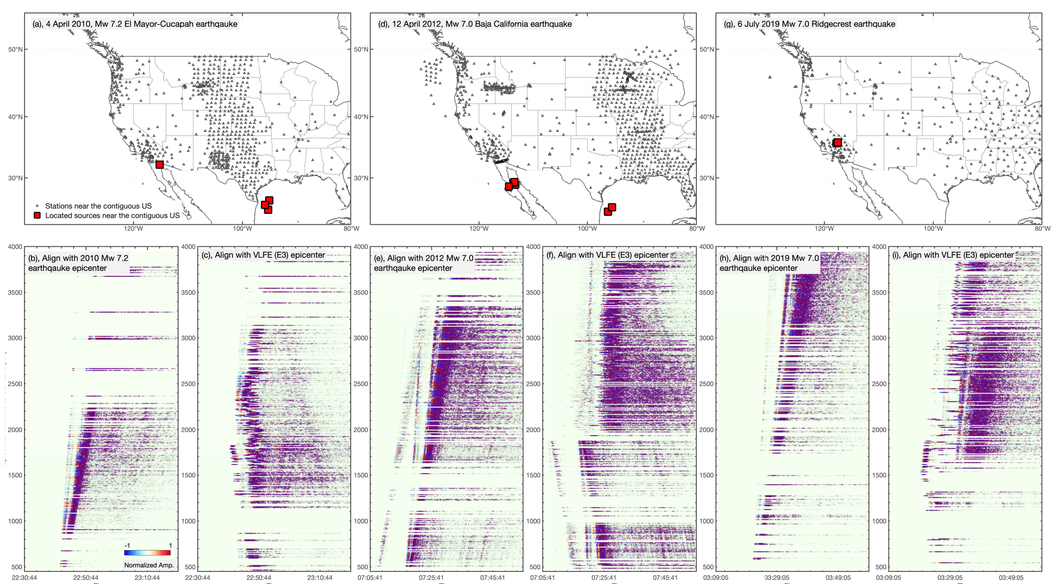


**Figure 9.** Detected seismic sources on 4 April 2010 (a), 12 April 2012 (d), and 6 July 2019 (g) and seismic records of the 2010 Mw 7.2 El Mayor-Cucapah earthquake (b–c), the 2012 Mw 7.0 Baja California earthquake (e–f), and the 2019 Mw 7.0 Ridgecrest earthquake (h–i). The record sections are one-hour record sections that are aligned with the earthquake epicenters (b, e, h) and the epicenter of the VLFE E3 (c, f, i). The legends are similar to those of Figure 3. Both the 2010 Mw 7.2 El Mayor-Cucapah earthquake and the 2012 Mw 7.0 Baja California earthquake triggered submarine landslides (a, d) in the Gulf of Mexico [*Fan et al.*, 2020].